

# Self-Powered Intelligent Water Meter for Electrostatic Scale Preventing, Rust Protection, and Flow Sensor in a Solar Heater System

Weichao Wang,<sup>†</sup> Yonghui Wu,<sup>†</sup> Zhenghu Chang,<sup>†</sup> Fangqi Chen,<sup>†</sup> Heyi Wang,<sup>†</sup> Guangqin Gu,<sup>‡</sup> Haiwu Zheng,<sup>\*,†</sup> Gang Cheng,<sup>\*,‡</sup> and Zhong Lin Wang<sup>\*,§,||,⊥</sup>

<sup>†</sup>Henan Key Laboratory of Photovoltaic Materials, School of Physics and Electronics and <sup>‡</sup>Key Lab for Special Functional Materials, Ministry of Education, Henan University, Kaifeng 475004, China

<sup>§</sup>Beijing Institute of Nanoenergy and Nanosystems, Chinese Academy of Sciences, Beijing 100083, China

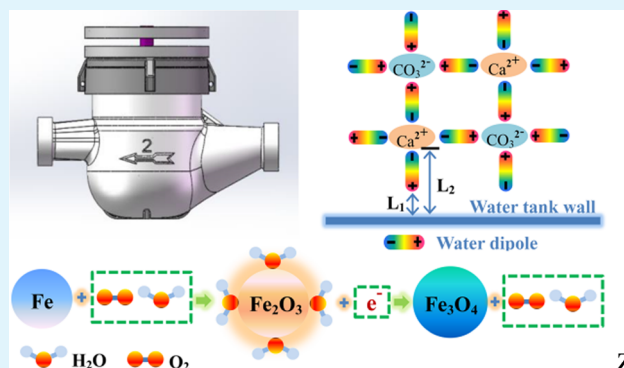
<sup>||</sup>School of Nanoscience and Technology, University of Chinese Academy of Sciences, Beijing 100049, China

<sup>⊥</sup>School of Materials Science and Engineering, Georgia Institute of Technology, Atlanta, Georgia 30332-0245, United States

## Supporting Information

**ABSTRACT:** Triboelectric nanogenerators (TENGs) have been investigated for mechanical energy harvesting because of their high-energy conversion efficiency, low cost, ease of manufacturing, and so on. This paper deals with designing a kind of water-fluid-driven rotating TENG (WR-TENG) inspired by the structure of a water meter. The designed WR-TENG is effectively integrated into a self-powered electrostatic scale-preventing and rust protection system. The WR-TENG can generate a constant DC voltage up to about 7.6 kV by using a voltage-doubling rectifier circuit (VDRC) to establish a high-voltage electrostatic field in the water tank. A WR-TENG, a VDRC, and an electric water heating tank are the components of the whole system. The system is convenient to be installed in any waterway system, effectively preventing the rusting of stainless steel and restraining the formation of scale when the water is heated to  $65 \pm 5$  °C. Moreover, the approximately linear relationship between the short-circuit current and the rotation rate of the WR-TENG makes employing it as a self-powered water flow sensor possible. This work enables a facile, safe, and effective approach for electrostatic scale prevention, rust protection, and flow sensing in solar heaters, which will enrich the high-voltage applications of TENGs.

**KEYWORDS:** triboelectric nanogenerator, self-powered water meter, scale prevention, rust protection, flow sensor



Many kinds of water heater systems, especially solar water heaters, are widely used in our daily life.<sup>1,2</sup> The scaling and corrosion in the solar water heater system after a long period of operation could affect its normal use and lifetime. This could be due to the lack of softening treatments. The scale removal of water systems is commonly based on chemical and physical methods.<sup>3–5</sup> The chemical scale removal method could cause secondary pollution to the environment because of the scale and waste liquid discharged from the water heaters. The physical scale removal methods usually require interrupting the operation of the water system, which may lead to damage to the pipeline and equipment. In another method, small electrostatic water processors using conventional power sources are installed on water systems. These electrostatic treatments have advantages of effectively preventing scaling, corrosion protection, and sterilization and do not cause secondary pollution to the environment.<sup>4–8</sup> However, the conventional power supply may cause electrical leakage and injury to people during the long-term operation of the solar

water heater system. Moreover, inconvenient power connection in the location of solar installation or some remote places could be considered as another drawback of the electrostatic-based scale-preventing methods.

In recent years, TENGs as a new power generation approach with the capability of converting various types of environmental mechanical energy into electricity based on the coupling of triboelectrification and electrostatic induction effects have been proposed.<sup>9,10</sup> To date, TENGs with different structures and working modes such as contact-separation mode,<sup>11–14</sup> sliding mode,<sup>15,16</sup> single-electrode mode,<sup>17–19</sup> and freestanding triboelectric-layer mode<sup>20–22</sup> have been developed. Among the four basic modes of TENGs, the contact freestanding mode has the advantage of good robustness and

Received: November 8, 2018

Accepted: January 17, 2019

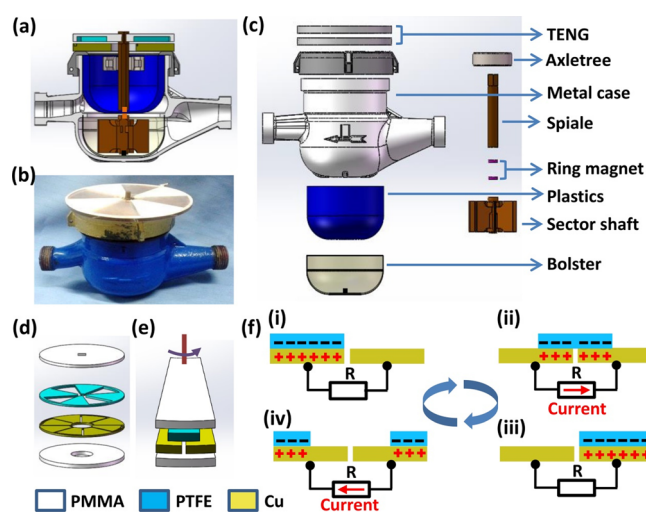
Published: January 17, 2019

figure of merit.<sup>23,24</sup> TENGs with multiple structural designs as a promising sustainable power source can be employed for energy harvesting from different environments, such as wind,<sup>25,26</sup> water wave,<sup>27–29</sup> water flow,<sup>30–33</sup> and biomechanical power energy.<sup>34–36</sup> High output energy and conversion efficiency, extremely low cost, ease of manufacture, light weight, and unique applicability are some advantages of the TENGs.<sup>9,37</sup> Generally, TENGs have high-voltage and low-current output characteristics. For the practical applications of self-powered sensors and low-power-consumption devices, it is highly necessary either to select a special transformer to convert the output of TENGs into low voltage with high current or to choose a rational energy storage unit to drive low-power micro/nanodevices. In addition, high-voltage applications of TENGs are one of their unique advantages, which are still at the initial stage.<sup>38–40</sup> In particular occasions, such as electrostatic scale prevention and rust protection in solar water heater systems, higher output voltage than that from the TENG itself regardless of the current magnitude is required. Electrostatic scale prevention necessitates us to generate a high-voltage electrostatic field in the water tank (up to 10 kV) while the current magnitude could be ignored.

In this work, a WR-TENG is developed by using the water meter structure that could be conveniently installed in any waterway system. The electric output of the mentioned WR-TENG is studied under different water flow rates. It works in a freestanding mode and is propelled by the water fluid in the pipe. It has the largest output voltage ( $V_{oc}$ ) about 420 V, an output current ( $I_{sc}$ ) about 9.32  $\mu$ A, a transferred charge ( $Q_{sc}$ ) about 150 nC, and a maximum instantaneous power of 1.61 mW at an optimum external load of 100 M $\Omega$ . The whole electrostatic scale-preventing and rust protection solar water heater system consists of a WR-TENG, a voltage-doubling rectifier circuit (VDRC), and a water tank heating system. The VDRC is employed to amplify the voltage generated from the WR-TENG, and then a maximum constant DC voltage of 7.6 kV can be obtained, which can establish a high-voltage electrostatic field in the water tank. The experimental results indicate that the system can effectively prevent rusting of stainless steel and the formation of scale on the water tank wall when the water tank is heated to  $65 \pm 5$  °C without any external power source. The electricity leakage and inconvenient power connection caused by traditional energy sources in the electrostatic scale prevention of solar heater water systems could be resolved using the proposed WR-TENG. Moreover, this WR-TENG has the ability to be utilized as a water flow sensor because of the approximately linear relationship between its short-circuit current and rotational speed. This could increase its potential applications in the future.

## RESULTS AND DISCUSSION

A schematic and structural design of the WR-TENG is shown in Figure 1. A sectional view of the WR-TENG and its photograph are shown in Figure 1a,b, respectively. The WR-TENG is mainly composed of a TENG working in freestanding triboelectric-layer mode and a transmission device, including a series of components, as shown in Figure 1c. A complete drawing of the assembled WR-TENG is shown in Figure S1a. The structural design of the two friction layers of the TENG is shown in Figure 1d. The photographs of the two complementary-patterned Cu-electrode networks and the poly(tetrafluoroethylene) (PTFE) layer including four alter-



**Figure 1.** Structural design and schematic of the operation principle of the WR-TENG. (a) Sectional view and (b) photograph of the WR-TENG. (c) The components of the WR-TENG. (d) Structural design of the two friction layers. (e) A basic unit of the WR-TENG. (f) Four processes illustrating the charge distribution and electricity generation: (i) initial state, fully aligned position; (ii) intermediate state, two surfaces are sliding apart; (iii) final state, fully mismatched position; and (iv) next intermediate state, two surfaces are sliding back together.

nate sectors on the poly(methyl methacrylate) (PMMA) substrate are shown in Figure S1b,c, respectively. The inductively coupled plasma (ICP) technique is applied to create nanostructures on the surface of the PTFE film for increasing the surface triboelectric charge density.<sup>41</sup> The scanning electron microscopy (SEM) image of PTFE with surface nanostructures is given in Figure S1d.

The basic unit of the WR-TENG is shown in Figure 1e. Figure 1f shows that the WR-TENG operates in the freestanding mode by the relative rotation between the rotator and the stator. When water flows through the transmission device, the sector shaft with a ring magnet will be driven by the flow of water to turn. Meanwhile, the spiale with a ring magnet will also turn due to the attraction principle in terms of the opposite polarity between the two ring magnets. This drives the freestanding triboelectric-layer fixed at the top of the spiale to rotate. According to triboelectrification and electrostatic induction effects, the relative rotation between the rotator and the stator will bring about an alternating flow of charges between the two electrode networks. As seen in Figure 1f, the electricity generation process is performed by the basic unit, from which the short-circuit current and charge distribution of the TENG are illustrated by a four-stage process. According to the charge conservation law, at the initial state, the positive charges on the stator electrodes are equal to the negative charges on the PTFE of the rotator to maintain electrostatic equilibrium (Figure 1fi). Figure 1fii shows that the mentioned electrostatic equilibrium between the two electrodes could be broken by rotating the rotor from the initial state to the transition state. Consequently, positive charges on the left electrode flow to the right electrode in the stator through the external circuit driven by the electrostatic potential difference. In this circumstance, the voltage reaches the maximum forward  $V_{oc}$ . When the rotor further spins to the state shown in Figure 1fiii, the positive charges on the right electrode are in equilibrium with the negative charges on the PTFE, and the

voltage decreases to zero. In the final state (Figure 1f iv), the voltage reaches the maximum reverse  $V_{oc}$ . Because the rotator continues to rotate, the electricity potential of the TENG periodically changes between the two electrodes.

For quantitative study of the output performance of the WR-TENG under different water flow rates, the WR-TENG is installed on the water pipe; refer to Movie S1 for the testing process. Figure 2 shows the  $V_{oc}$ ,  $I_{sc}$  and  $Q_{sc}$  of the WR-TENG

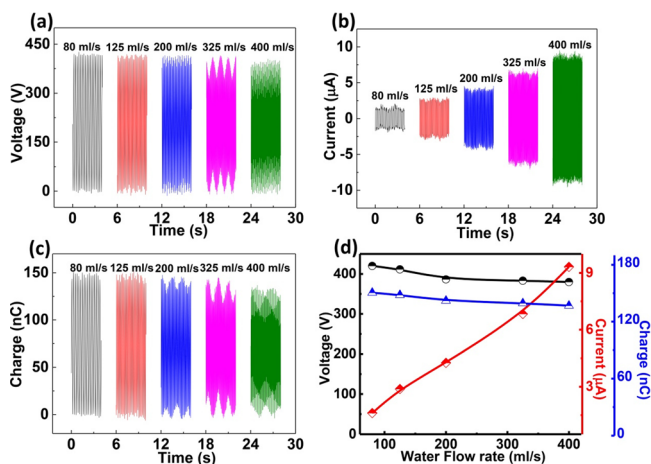


**Figure 2.** Electrical output performance of a WR-TENG under different water flow rates. (a) Open-circuit voltage, (b) short-circuit current, and (c) transferred charge. (d) Dependence of the  $V_{oc}$ ,  $I_{sc}$  and  $Q_{sc}$  on water flow rate.

with the water flow rate varying from 80 to 400 mL/s. According to Figure 2a,c, the water flow increase from 80 to 400 mL/s leads to a decrease in maximum values of  $V_{oc}$  and  $Q_{sc}$  from about 420 V and 150 nC to about 379 V and 136 nC, respectively, which indicates that the  $V_{oc}$  and the  $Q_{sc}$  have a slight decay with the increase of water flow rate. As we know, there is a linear relationship between the flow rate and the speed of the impeller in the rotating-vane-type water meter.<sup>42</sup> Therefore, increasing the water flow rate results in the increase of the rotator speed of the WR-TENG. A slight decay in the  $V_{oc}$  and the  $Q_{sc}$  at high rotational speed occurs, which might stem from the relatively low sampling rate of the voltage/charge meter.<sup>43,44</sup> Actually, the output voltage and the transferred charge should be mainly determined by the separated area of a single sector and not be influenced by the water flow rate, as shown from Figure 2d. Unlike the  $V_{oc}$  and  $Q_{sc}$ , increasing the water flow rate increases the amplitude of the  $I_{sc}$  (from  $\sim 1.61$  to  $\sim 9.32 \mu A$ ), as indicated in Figure 2b. The approximately linear relationship between the current and the water flow rate could be clearly found in Figure 2d. This linearity is mainly due to a boost in charge transfer rate caused by the enhancement in the water flow rate.

To investigate the maximum output power of the WR-TENG under different water flow rates, the effect of external resistance on the electric outputs of the WR-TENG is verified in Figure 3. It could be seen from Figure 3a–e that an increase in the external resistance (for different water flow rates) results in an increase in the output voltage and a decrease in the output current. The instantaneous output power of the WR-TENG obtained from the voltage and current output values is plotted in terms of the external resistance ranging from 1 k $\Omega$  to 2 G $\Omega$  in Figure 3f. According to Figure 2, the increase of the water flow rate can elevate  $I_{sc}$  while the value of  $V_{oc}$  remains

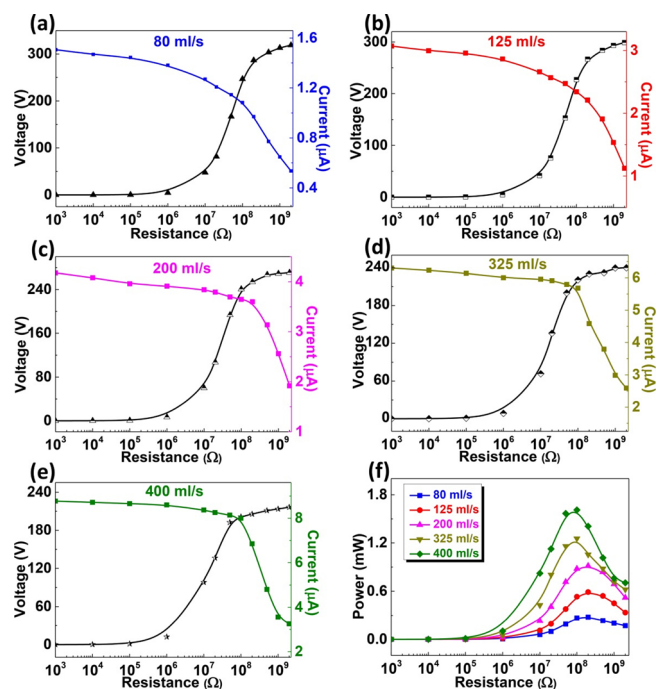


**Figure 3.** Output power performances of the WR-TENG at different water flow rates. (a–e) Output voltages and currents for different external resistance loads. (f) The instantaneous power in terms of external load resistance.

almost unchanged. Accordingly, the maximum value of the instantaneous power increases from  $\sim 0.28$  to  $\sim 1.61$  mW by increasing the water flow rate from 80 to 400 mL/s, and the corresponding optimum load resistance value decreases from 200 to 100 M $\Omega$ . This decrease is due to the increase in rotation speed of the WR-TENG caused by the increase in the water flow rate. Increasing the rotational rate is equal to enhancing the high-frequency component of  $V_{oc}$ , which will also decrease the WR-TENG impedance.<sup>45,46</sup> Consequently, the optimum matched resistance will reduce.

To demonstrate the capability of the WR-TENG as a sustainable power source, different commercial capacitors (470, 4700, and 10000 pF) were charged by the WR-TENG at the water flow rate of 325 mL/s (about 1.8 m/s). In accordance with Figure S2 (the inset shows the charging circuit diagram), larger capacitors require more charging time. However, all of the capacitor voltages are higher than the measuring range of the electrometer within 2 s because of the excellent output performance of the WR-TENG. Thus, an equivalent charging circuit is designed for capacitor charging. As seen from Figure 4a, the capacitor voltages reach their steady state value (about 700 V) within 5 s. However, several hundred volts is far from the required high DC voltage (a few to a dozen kilovolts) for an electrostatic scale removal system. Therefore, a VDRC without an external power source including a regular arrangement of diodes and capacitors ( $C_1 = C_2 = \dots = C_{14} = 470$  nF) was designed to overcome this problem in which its circuit diagram is shown in Figure 4b. The detailed working mechanism of the VDRC can be referred to in ref 34, and multiple DC voltages will be obtained at the two ends of the capacitor pack. The relationship between the obtained output voltage and the amplifying multiple of the WR-TENG is given in Figure 4c. The output voltage of the VDRC ( $V_{out}$ ) increases by increasing the amplifying multiple.

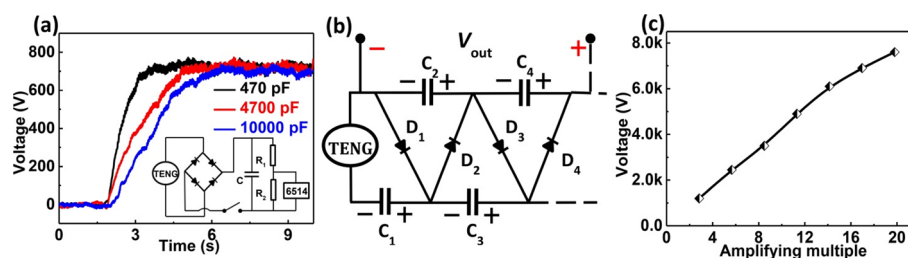


**Figure 4.** Electrical characteristics of the WR-TENG. (a) Charging curves obtained by the WR-TENG through a bridge rectifier for different values of capacitors. Inset: The charging circuit diagram ( $R_1 = 5 \text{ G}\Omega$ ,  $R_2 = 500 \text{ M}\Omega$ ). (b) Electrical circuit of the VDRC ( $C_1 = C_2 = \dots = C_{14} = 470 \text{ nF}$ ). (c) Output voltage of the VDRC ( $V_{\text{out}}$ ) in terms of the amplifying multiple.

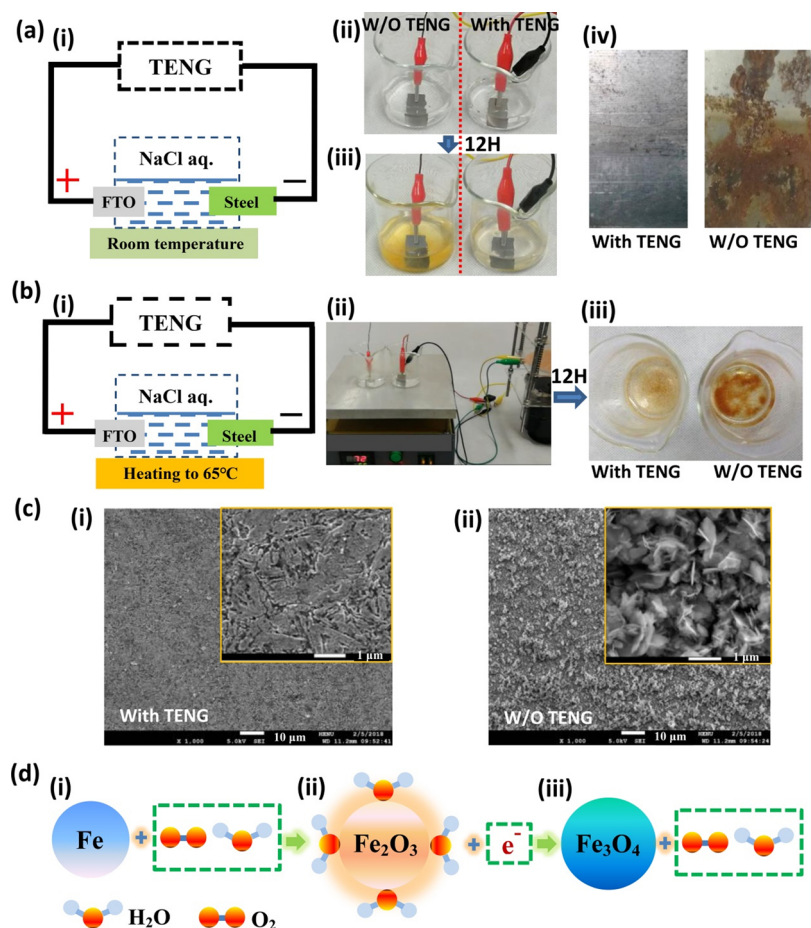


**Figure 5.** Self-powered electrostatic rust protection. (a) System diagrams and photographs at room temperature: (i) the circuit diagram for electrochemical protection by the WR-TENG and (ii, iii) photographs for rust protection of the stainless steel with and without the TENG at the initial stage and after 12 h, respectively, and (iv) picture contrast of the surface morphology for the steel with and without the TENG after 12 h. (b) System diagrams and photographs at  $65 \pm 5 \text{ }^\circ\text{C}$ : (i, ii) the circuit diagram and photographs of rust protection, respectively, and (iii) photograph contrast of formed rust with and without the TENG at  $65 \pm 5 \text{ }^\circ\text{C}$  for 12 h. (c) SEM image of the steel surface (i) with and (ii) without the TENG after keeping the temperature at  $65 \pm 5 \text{ }^\circ\text{C}$  for 12 h, respectively. (d) Schematic diagram of the chemical reactions for rust protection. The proposed chemical reaction process was described as states (i), (ii), and (iii).

The maximum attainable output voltage is 7.6 kV at the maximum magnification of the designed VDRC. It is compatible with the demand for a self-powered high-voltage electrostatic scale-preventing system.

To demonstrate the capability of the WR-TENG as a sustainable power source, commercial LEDs were connected to the WR-TENG in series, which are assembled to form the word "HENU" and continuously powered by the WR-TENG installed on a water pipe. All of the LEDs could be readily lit up once the water pipe switch is opened (Movies S2). The

performance of the self-powered electrostatic rust protection system has been investigated at room temperature and  $65 \pm 5 \text{ }^\circ\text{C}$ , as shown in Figure 5. To save water resources, the same size WR-TENG onto the PMMA substrate (length: 12 cm; width: 12 cm; height: 3 mm) is re-fabricated, and four holes were drilled on the edge of the PMMA sheet, and mounted on a motor using screws to drive the TENG rotor. A bridge rectifier is employed to convert the AC outputs into DC for facilitating the performance test of the metal corrosion. Figure 5a describes the circuit diagram for electrochemical protection of

stainless steel utilized by the WR-TENG at room temperature. When commercial stainless steel (SUS304) used in solar water heater tanks was immersed in NaCl aqueous solution (0.1 mmol/L), it will be corroded in 2 h without connection to the TENG device. However, the transferred electrons are injected into the protected steel when the steel is connected to the TENG device, which can effectively suppress metal corrosion. It is obvious from Figure Siii–iv that the steel connected to the TENG is almost not corroded, but the steel not connected to the TENG is severely corroded after 12 h of immersion, and detailed experimental progress is shown in Figure S3 and Movies S3.

It is well known that the water temperature in the solar water heater is usually higher than room temperature. Therefore, the metal corrosion performance with and without the TENG at  $65 \pm 5^\circ\text{C}$  was investigated. Figure 5bi,ii shows the circuit diagram and physical drawing, respectively, for the protection of the steel with the WR-TENG at high temperature. As depicted in Figure 5biii, the steel connected to the TENG has less rust than that not connected to the TENG. Consequently, it is inferred that although the corrosion of the steel at high temperature is more serious than that at room temperature, the WR-TENG could slow down the corrosion rate of stainless steel. Figure 5c shows the SEM images of the steel connected or not to the TENG after immersion for 12 h at  $65 \pm 5^\circ\text{C}$ . It is obvious that the TENG favors the formation of a dense protective layer on the surface of stainless steel. More optical images and an additional video for the rust protection progress of the steel with and without the TENG for different time values are shown in Figure S4 and Movie S4. The antirust mechanism of the steel with the TENG is given in Figure 5d. When stainless steel is immersed in the NaCl aqueous solution (state i), the steel absorbs oxygen and loses electrons, reacting with  $\text{O}_2$  and  $\text{H}_2\text{O}$  to form  $\text{Fe}(\text{OH})_2$ , which forms rust ( $\text{Fe}_2\text{O}_3 \cdot x\text{H}_2\text{O}$ ) after oxidation (state ii). Connecting the TENG to the steel leads to a large number of electrons to be injected into the stainless steel. This prevents the oxygen inhalation reaction and results in corrosion inhibition (state iii). Because of the production of  $\text{Fe}_3\text{O}_4$  formed by the reaction of  $\text{Fe}_2\text{O}_3 \cdot x\text{H}_2\text{O}$  and injected electrons, the corrosion can be suppressed even if the surface of the steel is partially corroded in the initial state.<sup>47,48</sup> In other words, the surface reaction of the steel immersed in the NaCl solution is suppressed because of the injected electrons at room temperature, preventing the formation of rust. At high temperature, the steel reacted with the injected electrons to produce  $\text{Fe}_3\text{O}_4$ , impeding the formation of rust and postponing the corrosion of the steel.

To further extend the application of the WR-TENG, an electric water heater tank was designed for simulation of the solar water heater, and the scale-preventing performance of the WR-TENG was investigated. Figure 6a shows the system diagram of the self-powered electrostatic scale-preventing system, including a WR-TENG, a VDRC, and a solar water heater. Water flow through the WR-TENG drives the rotator of the TENG to turn and generate electricity. The generated electricity is amplified by the VDRC rectifier to generate a high-voltage electrostatic field (about 7.6 kV) in the solar water heater for preventing the scale formation. Finally, a high-voltage electrostatic field is generated between the electrostatic ion-stick and the water tank wall. The structural diagram of the electrostatic ion-stick is shown in Figure S5. As could be seen from Figure 6bi, the positive pole and the negative pole of the

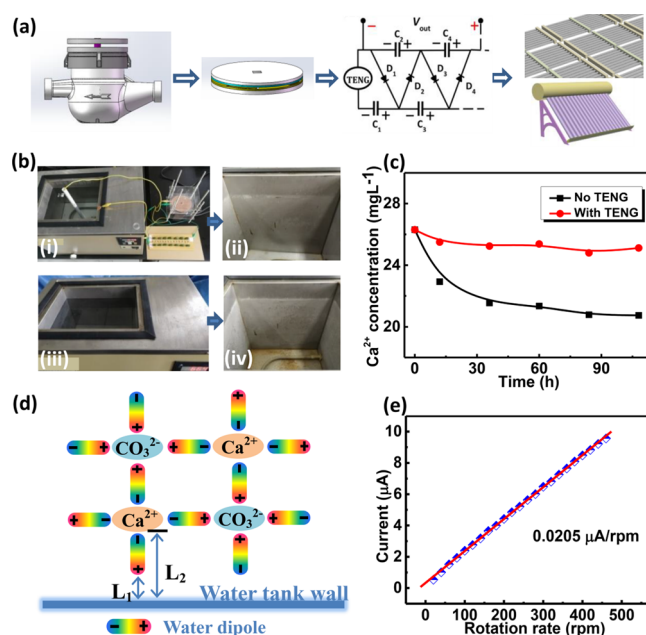


**Figure 6.** Application of the self-powered electrostatic scale-preventing system. (a) Diagram of the self-powered electrostatic scale-preventing system. (b) Photographs of (i) the scale-preventing system combined with the TENG, (ii) the water tank wall with the TENG after 108 h of testing at  $65 \pm 5^\circ\text{C}$ , (iii) the water tank without the TENG, and (iv) the water tank wall without the TENG after 108 h of testing at  $65 \pm 5^\circ\text{C}$ . (c)  $\text{Ca}^{2+}$  concentration variations with and without the TENG. (d) Array of water molecules and anions under electrostatic conditions ( $L_1 < L_2$ ). (e) Dependence of the  $I_{sc}$  of the WR-TENG on the rotation rate.

VDRC are connected to the electrostatic ion-stick and water tank wall, respectively. To implement the solar water heater, 10 L of water was poured into the water tank, heated to keep the water temperature at about  $65 \pm 5^\circ\text{C}$  for 12 h. Then, a water sample of 15 mL is taken. After draining off 5 L of water, 5 L of fresh tap water is added to simulate the use of the water heater. Sampling is repeated every 24 h in the next 96 h according to the abovementioned procedure. This is done to examine the calcium ion content of the water samples using atomic absorption spectroscopy. The photographs of comparative test of the experimental effect for scale prevention and the  $\text{Ca}^{2+}$  concentration of the samples with and without the WR-TENG are shown in Figure 6b,c, respectively. It is obvious from Figure 6bii,iv that the amounts of white scale formed on the water tank wall are less and more with and without the WR-TENG, respectively, after 108 h. Moreover, some rust is observed at the bottom of the water tank without the WR-TENG, which is consistent with the experimental result described in Figure 5biii.

Figure 6c shows that the  $\text{Ca}^{2+}$  concentration of the sample connected to the WR-TENG is significantly higher than the corresponding one not connected to the WR-TENG. The test data are shown in Table S1. These experimental results indicate that the WR-TENG can effectively obstruct the deposition of  $\text{Ca}^{2+}$  and thus inhibit the scale formation in the solar heater. Taken  $\text{CaCO}_3$  as an example, the principle of scale inhibition by an ion-stick electrostatic water treater is illustrated in Figure 6d, which shows the array layout of water molecules and ions under electrostatic conditions ( $L_1$  and  $L_2$  are the distances from the ion to the inner water tank wall). The water molecules are affected by the high-voltage

electrostatic field between the electrostatic ion-stick and the wall of the water tank, forming water dipoles, by which the cations and anions from dissolved salts will be surrounded. Consequently, the cations contained in the water do not tend to gather on the wall of the water tank.<sup>4–6</sup> Thus, the scale prevention purpose is realized. Although high-voltage application of rotating-disk TENGs (R-TENGs) has been reported to power the electrospinning system, the rotation rate of the R-TENG is as high as 1200 rpm.<sup>34</sup> Generally, the rotation rate of R-TENGs driven by natural wind or water flow is relatively low. Because the rotation rate of the WR-TENG in the current case is not higher than 500 rpm, it is reasonably inferred that the WR-TENG installed on any water pipes is more suitable for large-scale applications, serving for the self-powered electrostatic scale-preventing system. More importantly, as far as we know, it is the first time that the high-voltage application of the TENG in the area of environmental electrochemistry has been demonstrated.

Figure 6e represents the variations of  $I_{sc}$  of the WR-TENG in terms of the rotation rate. Moreover, the  $I_{sc}$  values of the WR-TENG with different rotation rates varying in the range from 20 to 460 rpm are shown in Figure S6. It is obvious that the relationship between  $I_{sc}$  of the WR-TENG and the rotation rate is approximately linear. The obtained sensitivity is about  $0.0205 \mu\text{A}/\text{rpm}$ . In addition, the relationship between the rotational speed of the WR-TENG and the water flow is almost linear. Therefore, the WR-TENG could be used as a self-powered intelligent water meter to detect and monitor the velocity and flow of water in water pipes.

## CONCLUSIONS

In this paper, the water meter structure is employed to design a kind of water-fluid-driven rotating triboelectric nanogenerator that could be installed in any waterway system. The relationship between the output performance of the WR-TENG and the water flow rate is studied. An appropriate VDRC is designed to generate a constant DC voltage up to about 7.6 kV. This leads to a high-voltage electrostatic field in the water tank preventing stainless steel rusting and scale formation in its wall when the water is heated at  $65 \pm 5 \text{ }^\circ\text{C}$ . The leakage injury caused by a conventional power supply and inappropriate power supply connection in the solar installation location or a remote area could be resolved by employing the WR-TENG in solar water heater systems. Moreover, the WR-TENG could also be employed as an intelligent water meter for real-time monitoring of water flow. The WR-TENG provides a novel supplement to utilize water flow energy for electrostatic scale prevention, rust protection, and flow sensing in solar heaters with no additional power supplies required, which will lead to an important breakthrough in self-powered electrostatic scale-preventing technology in the future.

## EXPERIMENTAL SECTION

**Fabrication Process of the Transmission Device.** First, the sector shaft and counting part of a commercial water meter were disassembled and removed. Second, a sector rotation shaft with a size corresponding to that of the original water meter was reprinted by 3D-printing technology. The upper diameter of the middle cylinder is 8 mm, which could be embedded into a purchased ring magnet. At the same time, a spiale containing a tip at the bottom, a square column at the top, and a cylinder in the middle is designed using the SOLIDWORKS software and printed using a 3D printer. The diameter and height of the central cylinder are 8 and 58 mm, respectively. Moreover, the side length and height of the upper square

column are 5 and 8 mm, respectively. Then, a ring magnet is embedded into the spiale bottom. Third, the device is reassembled according to the water meter structure, and a bearing is fixed on the spiale on the top of the meter. Then, a PMMA plate with a copper electrode as the stator is fixed to the top of the water meter. Moreover, the other PMMA with a PTFE friction layer as the rotor is fixed to the square column. Finally, a kind of rotating triboelectric nanogenerator driven by water fluid is successfully developed.

**Preparation of TENG.** The TENG mainly consists of two parts: a stator and a rotor. For the stator, a PMMA sheet as the supporting substrate with 100 mm diameter and 3 mm thickness cut by a laser cutter is employed. A hole with 10 mm diameter is created at the substrate center. Afterward, copper foil with 100 mm width and 0.065 mm thickness is provided as a friction layer. Then, the electrode is adhered onto the PMMA substrate. Under the assistance of a PMMA mold, the two complementary-patterned Cu electrodes are separated by a blade with fine equal intervals with  $3^\circ$  central angle. When the electrodes are mutually connected by four copper units at one end, the electrode network is formed. To build the rotor, another PMMA sheet with 100 mm diameter and 1 mm thickness as a supporting substrate cut by a laser cutter is utilized. By cutting the substrate center, a square hole with 5 mm side length is created. After that, a PTFE film is utilized as a friction layer to stick on the PMMA substrate. A blade with the aid of a PMMA mold is employed for cutting the PTFE film into eight uniformly arranged sectors and removing four alternate sectors from the PMMA substrate. Finally, for fabricating the TENG, the stator and the rotor are installed on the top of the water meter and the square column of the spiale, respectively. Moreover, two lead wires are employed from the two Cu electrode networks.

**Measurements.** The output voltage, output current, and transfer charge of the WR-TENG are measured using an electrometer (Keithley6514). The water flow rate is calculated by the water flow volume per time. Scanning electron microscopy (SEM, JSM-7001F) is utilized for morphology characterization of the surface of the PTFE and steel.  $V_{out}$  is measured by a non-contacting electrostatic probe (Trek-523) because it is far beyond the detection range of the electrometer. The calcium ion concentration in tap and hot water is measured using a flame method by atomic absorption spectroscopy (HITACHI, Z-2000).

## ASSOCIATED CONTENT

### Supporting Information

The Supporting Information is available free of charge on the ACS Publications website at DOI: 10.1021/acsami.8b19683.

Drawing and photographs of the WR-TENG, charging curves of different capacitors, metal corrosion protection performance at room temperature and heating up to  $65 \pm 5 \text{ }^\circ\text{C}$ , structural diagram of ion-stick electrostatic,  $I_{sc}$  of the TENG at different rotation rates, and contrast test for scale prevention (PDF)

Measurement of the output performance of the WR-TENG installed on the water pipe (AVI)

Lighting up of green LEDs connected in series forming the word "HENU" and connected to the TENG installed on the water pipe (AVI)

Performing metal corrosion protection at room temperature (AVI)

Performing metal corrosion protection at a temperature of  $65 \pm 5 \text{ }^\circ\text{C}$  (AVI)

## AUTHOR INFORMATION

### Corresponding Authors

\*E-mail: zhenghaiw@ustc.edu (H.Z.).

\*E-mail: chenggang@henu.edu.cn (G.C.).

\*E-mail: zlwang@gatech.edu (Z.L.W.).

ORCID 

Haiwu Zheng: 0000-0002-2021-4159

Gang Cheng: 0000-0002-1242-8739

Zhong Lin Wang: 0000-0002-5530-0380

## Author Contributions

The manuscript was written with contributions from all authors. All authors have given approval to the final version of the manuscript.

## Notes

The authors declare no competing financial interest.

## ACKNOWLEDGMENTS

The authors gratefully acknowledge the support from the National Key Research and Development of China (Grant No. 2016YFA0202704), the National Natural Science Foundation of China (No. 51872074, 51432005 and 61522405), the Scientific and Technological Project in Henan Province (172102210013), and the Program for Innovative Research Team in Science and Technology in University of Henan Province (19IRTSTHN019).

## REFERENCES

- (1) Gupta, C. L.; Garg, H. P. System Design in Solar Water Heaters with Natural Circulation. *Sol. Energy* **1968**, *12*, 163–182.
- (2) Jaisankar, S.; Radhakrishnan, T. K.; Sheeba, K. N. Experimental Studies on Heat Transfer and Friction Factor Characteristics of Thermosyphon Solar Water Heater System Fitted with Spacer at the Trailing Edge of Twisted Tapes. *Appl. Therm. Eng.* **2009**, *29*, 1224–1231.
- (3) Xyla, A. G.; Mikroyannidis, J.; Koutsoukos, P. G. The Inhibition of Calcium Carbonate Precipitation in Aqueous Media by Organophosphorus Compounds. *J. Colloid Interface Sci.* **1992**, *153*, 537–551.
- (4) Busch, K. W.; Busch, M. A. Laboratory Studies on Magnetic Water Treatment and Their Relationship to a Possible Mechanism for Scale Reduction. *Desalination* **1997**, *109*, 131–148.
- (5) Cho, Y. I.; Fan, C.; Choi, B.-G. Use of Electronic Anti-Fouling Technology with Filtration to Prevent Fouling in a Heat Exchanger. *Int. J. Heat Mass Transfer* **1998**, *41*, 2961–2966.
- (6) Qiu, Q. T.; Liu, S. S.; Huang, Y. X.; Liu, X. Y. A Technique to Save Energy Scale Control by Physical Fields. *Physics* **2002**, *31*, 162–166.
- (7) Kim, J.-G.; Joo, J.-H.; Koo, S.-J. Development of High-Driving Potential and High-Efficiency Mg-Based Sacrificial Anodes for Cathodic Protection. *J. Mater. Sci. Lett.* **2000**, *19*, 477–479.
- (8) Ye, C.-Q.; Hu, R.-G.; Dong, S.-G.; Zhang, X.-J.; Hou, R.-Q.; Du, R.-G.; Lin, C.-J.; Pan, J.-S. EIS Analysis on Chloride-Induced Corrosion Behavior of Reinforcement Steel in Simulated Carbonated Concrete Pore Solutions. *J. Electroanal. Chem.* **2013**, *688*, 275–281.
- (9) Wang, Z. L. Triboelectric Nanogenerators as New Energy Technology for Self-Powered Systems and as Active Mechanical and Chemical Sensors. *ACS Nano* **2013**, *7*, 9533–9557.
- (10) Zhang, L.; Jin, L.; Zhang, B.; Deng, W.; Pan, H.; Tang, J.; Zhu, M.; Yang, W. Multifunctional Triboelectric Nanogenerator Based on Porous Micro-Nickel Foam to Harvest Mechanical Energy. *Nano Energy* **2015**, *16*, 516–523.
- (11) Zhu, G.; Pan, C.; Guo, W.; Chen, C.-Y.; Zhou, Y.; Yu, R.; Wang, Z. L. Triboelectric-Generator-Driven Pulse Electrodeposition for Micropatterning. *Nano Lett.* **2012**, *12*, 4960–4965.
- (12) Zhong, Q.; Zhong, J.; Hu, B.; Hu, Q.; Zhou, J.; Wang, Z. L. A Paper-Based Nanogenerator as a Power Source and Active Sensor. *Energy Environ. Sci.* **2013**, *6*, 1779–1784.
- (13) Ding, W.; Wu, C.; Zi, Y.; Zou, H.; Wang, J.; Cheng, J.; Wang, A. C.; Wang, Z. L. Self-Powered Wireless Optical Transmission of Mechanical Agitation Signals. *Nano Energy* **2018**, *47*, 566–572.
- (14) Chen, S.; Wu, N.; Ma, L.; Lin, S.; Yuan, F.; Xu, Z.; Li, W.; Wang, B.; Zhou, J. Noncontact Heartbeat and Respiration Monitoring

Based on a Hollow Microstructured Self-Powered Pressure Sensor. *ACS Appl. Mater. Interfaces* **2018**, *10*, 3660–3667.

- (15) Zhu, G.; Su, Y.; Bai, P.; Chen, J.; Jing, Q.; Yang, W.; Wang, Z. L. Harvesting Water Wave Energy by Asymmetric Screening of Electrostatic Charges on a Nanostructured Hydrophobic Thin-Film Surface. *ACS Nano* **2014**, *8*, 6031–6037.
- (16) Zhu, G.; Zhou, Y. S.; Bai, P.; Meng, X. S.; Jing, Q.; Chen, J.; Wang, Z. L. A Shape-Adaptive Thin-Film-Based Approach for 50% High-Efficiency Energy Generation Through Micro-Grating Sliding Electrification. *Adv. Mater.* **2014**, *26*, 3788–3796.
- (17) Wang, X.; Wang, S.; Yang, Y.; Wang, Z. L. Hybridized Electromagnetic Triboelectric Nanogenerator for Scavenging Air-Flow Energy to Sustainably Power Temperature Sensors. *ACS Nano* **2015**, *9*, 4553–4562.
- (18) Niu, S.; Liu, Y.; Wang, S.; Lin, L.; Zhou, Y. S.; Hu, Y.; Wang, Z. L. Theoretical Investigation and Structural Optimization of Single-Electrode Triboelectric Nanogenerators. *Adv. Funct. Mater.* **2014**, *24*, 3332–3340.
- (19) Zhang, Q.; Liang, Q.; Liao, Q.; Yi, F.; Zheng, X.; Ma, M.; Gao, F.; Zhang, Y. Service Behavior of Multifunctional Triboelectric Nanogenerators. *Adv. Mater.* **2017**, *29*, 1606703.
- (20) Kuang, S. Y.; Chen, J.; Cheng, X. B.; Zhu, G.; Wang, Z. L. Two-Dimensional Rotary Triboelectric Nanogenerator as a Portable and Wearable Power Source for Electronics. *Nano Energy* **2015**, *17*, 10–16.
- (21) Gu, G. Q.; Han, C. B.; Lu, C. X.; He, C.; Jiang, T.; Gao, Z. L.; Li, C. J.; Wang, Z. L. Triboelectric Nanogenerator Enhanced Nanofiber Air Filters for Efficient Particulate Matter Removal. *ACS Nano* **2017**, *11*, 6211–6217.
- (22) Wang, S.; Xie, Y.; Niu, S.; Lin, L.; Wang, Z. L. Freestanding Triboelectric-Layer-Based Nanogenerators for Harvesting Energy from a Moving Object or Human Motion in Contact and Non-Contact Modes. *Adv. Mater.* **2014**, *26*, 2818–2824.
- (23) Li, S.; Wang, S.; Zi, Y.; Wen, Z.; Lin, L.; Zhang, G.; Wang, Z. L. Largely Improving the Robustness and Lifetime of Triboelectric Nanogenerators through Automatic Transition between Contact and Noncontact Working States. *ACS Nano* **2015**, *9*, 7479–7487.
- (24) Zi, Y.; Niu, S.; Wang, J.; Wen, Z.; Tang, W.; Wang, Z. L. Standards and Figure-of-Merits for Quantifying the Performance of Triboelectric Nanogenerators. *Nat. Commun.* **2015**, *6*, 8376.
- (25) Yang, Y.; Zhu, G.; Zhang, H.; Chen, J.; Zhong, X.; Lin, Z.-H.; Su, Y.; Bai, P.; Wen, X.; Wang, Z. L. Triboelectric Nanogenerator for Harvesting Wind Energy and as Self-Powered Wind Vector Sensor System. *ACS Nano* **2013**, *7*, 9461–9468.
- (26) Guo, H.; He, X.; Zhong, J.; Zhong, Q.; Leng, Q.; Hu, C.; Chen, J.; Tian, L.; Xi, Y.; Zhou, J. A Nanogenerator for Harvesting Air-flow Energy and Light Energy. *J. Mater. Chem. A* **2014**, *2*, 2079–2087.
- (27) Chen, J.; Yang, J.; Li, Z.; Fan, X.; Zi, Y.; Jing, Q.; Guo, H.; Wen, Z.; Pradel, K. C.; Niu, S.; Wang, Z. L. Networks of Triboelectric Nanogenerators for Harvesting Water Wave Energy: A Potential Approach toward Blue Energy. *ACS Nano* **2015**, *9*, 3324–3331.
- (28) Jiang, T.; Zhang, L. M.; Chen, X.; Han, C. B.; Tang, W.; Zhang, C.; Xu, L.; Wang, Z. L. Structural Optimization of Triboelectric Nanogenerator for Harvesting Water Wave Energy. *ACS Nano* **2015**, *9*, 12562–12572.
- (29) Yang, P.; Liu, K.; Chen, Q.; Li, J.; Duan, J.; Xue, G.; Xu, Z.; Xie, W.; Zhou, J. Solar-Driven Simultaneous Steam Production and Electricity Generation from Salinity. *Energy Environ. Sci.* **2017**, *10*, 1923.
- (30) Xie, Y.; Wang, S.; Niu, S.; Lin, L.; Jing, Q.; Su, Y.; Wu, Z.; Wang, Z. L. Multi-Layered Disk Triboelectric Nanogenerator for Harvesting Hydropower. *Nano Energy* **2014**, *6*, 129–136.
- (31) Liang, Q.; Yan, X.; Gu, Y.; Zhang, K.; Liang, M.; Lu, S.; Zheng, X.; Zhang, Y. Highly Transparent Triboelectric Nanogenerator for Harvesting Water-Related Energy Reinforced by Antireflection Coating. *Sci. Rep.* **2015**, *5*, 9080.
- (32) Zhang, Q.; Liang, Q.; Liao, Q.; Ma, M.; Gao, F.; Zhao, X.; Song, Y.; Song, L.; Xun, X.; Zhang, Y. An Amphiphobic Hydraulic

Triboelectric Nanogenerator for a Self-Cleaning and Self-Charging Power System. *Adv. Funct. Mater.* **2018**, *28*, 1803117.

(33) Ding, T.; Liu, K.; Li, J.; Xue, G.; Chen, Q.; Huang, L.; Hu, B.; Zhou, J. All-Printed Porous Carbon Film for Electricity Generation from Evaporation-Driven Water Flow. *Adv. Funct. Mater.* **2017**, *27*, 1700551.

(34) Pu, X.; Guo, H.; Chen, J.; Wang, X.; Xi, Y.; Hu, C.; Wang, Z. L. Eye Motion Triggered Self-Powered Mechnosensational Communication System Using Triboelectric Nanogenerator. *Sci. Adv.* **2017**, *3*, No. e1700694.

(35) Chinnappan, A.; Baskar, C.; Baskar, S.; Ratheesh, G.; Ramakrishna, S. An Overview of Electrospun Nanofibers and Their Application in Energy Storage, Sensors and Wearable/Flexible Electronics. *J. Mater. Chem. C* **2017**, *5*, 12657.

(36) Liao, X.; Zhang, Z.; Kang, Z.; Gao, F.; Liao, Q.; Zhang, Y. Ultrasensitive and Stretchable Resistive Strain Sensors Designed for Wearable Electronics. *Mater. Horiz.* **2017**, *4*, 502–510.

(37) Liu, G.; Chen, J.; Tang, Q.; Feng, L.; Yang, H.; Li, J.; Xi, Y.; Wang, X.; Hu, C. Wireless Electric Energy Transmission through Various Isolated Solid Media Based on Triboelectric Nanogenerator. *Adv. Energy Mater.* **2018**, *8*, 1703086.

(38) Cheng, J.; Ding, W.; Zi, Y.; Lu, Y.; Ji, L.; Liu, F.; Wu, C.; Wang, Z. L. Triboelectric Microplasma Powered by Mechanical Stimuli. *Nat. Commun.* **2018**, *9*, 3733.

(39) Li, A.; Zi, Y.; Guo, H.; Wang, Z. L.; Fernández, F. M. Triboelectric Nanogenerators for Sensitive Nano-Coulomb Molecular Mass Spectrometry. *Nat. Nanotech.* **2017**, *12*, 481–487.

(40) Li, C.; Yin, Y.; Wang, B.; Zhou, T.; Wang, J.; Luo, J.; Tang, W.; Cao, R.; Yuan, Z.; Li, N.; Du, X.; Wang, C.; Zhao, S.; Liu, Y.; Wang, Z. L. Self-Powered Electrospinning System Driven by a Triboelectric Nanogenerator. *ACS Nano* **2017**, *11*, 10439–10445.

(41) Wang, W.; Xu, J.; Zheng, H.; Chen, F.; Jenkins, K.; Wu, Y.; Wang, H.; Zhang, W.; Yang, R. A Spring-Assisted Hybrid Triboelectric-Electromagnetic Nanogenerator for Harvesting Low-Frequency Vibration Energy and Creating a Self-Powered Security System. *Nanoscale* **2018**, *10*, 14747–14754.

(42) Wu, G. B. The Flowrate Equation and Characteristic Curve Equation of the Vane-Wheel Water Meter. *J. Univ. Shanghai Sci. Tech.* **1987**, *9*, 12–21.

(43) Lin, L.; Wang, S.; Xie, Y.; Jing, Q.; Niu, S.; Hu, Y.; Wang, Z. L. Segmentally Structured Disk Triboelectric Nanogenerator for Harvesting Rotational Mechanical Energy. *Nano Lett.* **2013**, *13*, 2916–2923.

(44) Jing, Q.; Zhu, G.; Bai, P.; Xie, Y.; Chen, J.; Han, R. P. S.; Wang, Z. L. Case-Encapsulated Triboelectric Nanogenerator for Harvesting Energy from Reciprocating Sliding Motion. *ACS Nano* **2014**, *8*, 3836–3842.

(45) Niu, S.; Liu, Y.; Chen, X.; Wang, S.; Zhou, Y. S.; Lin, L.; Xie, Y.; Wang, Z. L. Theory of Freestanding Triboelectric-Layer-Based Nanogenerators. *Nano Energy* **2015**, *12*, 760–774.

(46) Niu, S.; Wang, S.; Lin, L.; Zhou, Y. S.; Hu, Y.; Wang, Z. L. Theoretical Study of Contact-Mode Triboelectric Nanogenerators as an Effective Power Source. *Energy Environ. Sci.* **2013**, *6*, 3576–3583.

(47) Zhu, H. R.; Tang, W.; Gao, C. Z.; Han, Y.; Li, T.; Cao, X.; Wang, Z. L. Self-Powered Metal Surface Anti-Corrosion Protection Using Energy Harvested from Rain Drops and Wind. *Nano Energy* **2015**, *14*, 193–200.

(48) Li, X.; Tao, J.; Guo, W.; Zhang, X.; Luo, J.; Chen, M.; Zhu, J.; Pan, C. A Self-Powered System Based on Triboelectric Nanogenerators and Supercapacitors for Metal Corrosion Prevention. *J. Mater. Chem. A* **2015**, *3*, 22663–22668.